Corrosion behaviour of Magnesium and Magnesium-Hydroxyapatite (Mg-HA) composite fabricated by friction stir processing in Dulbecco's phosphate buffered saline

D. Ahmadkhaniha[*a], M. Fedel [b], M. Heydarzadeh Sohi [a], A. Zarei Hanzaki [a], F. Deflorian [b]

a: School of Metallurgy and Materials, College of Engineering, University of Tehran, Tehran, PO Box 1155-4563, Iran, Telephone number: 00989126174090, email: ahmadkhany@ut.ac.ir

b: Department of Industrial Engineering, University of Trento, via Sommarive n. 9, 38123 Trento, Italy

Abstract

Magnesium-Hydroxyapatite (Mg-HA) composite was fabricated by friction stir processing (FSP). The effects of HA particles addition along with structural refinement on the corrosion resistance of Mg-HA composite in Dulbecco's phosphate buffered saline were then investigated. This was performed using electrochemical techniques and X-ray diffraction analysis. The results indicate that the achieved grain refinement (from approximately 1mm to 18 μm) and the dominated basal texture in friction stir processed magnesium would properly enhance its

corrosion resistance by more than one order of magnitude after 96 hours of immersion. However, the addition and embedding the HA particles would weaken the basal texture thereby deteriorating the corrosion resistance to less than 20% of the friction stir processed Mg.

Keywords: A: Magnesium; A: Metal matrix composites; B: EIS; B: Polarization; B: XRD

1. Introduction

Magnesium is well known as a biodegradable material [1] and it is potentially considered for bone substitute due to its relatively low Young's modulus and biocompatibility [1-3]. The major drawback of magnesium and its alloys is their high corrosion rate in the physiological environment with pH value around 7.4–7.6. This in fact reduces the mechanical integrity before ending the required period of bone tissue healing. Furthermore, the degradation of magnesium alloys may lead to hydrogen evolution and alkalization of the electrolyte. By decreasing the biodegradation rate of magnesium, the releasing rate of Mg^{2+}, H_2 and OH^- would be reduced and could allow sufficient time for human body to response to biodegradation products. The biodegradation rate of magnesium can be controlled in various ways, including alloying [4-6], surface treatment [7-9] and forming magnesium-matrix composites (MMCs) [1, 10-24]. A few studies on improving the corrosion resistance of magnesium implants by means of MMCs have been reported in the literature. Feng et al. [13] fabricated calcium polyphosphate (CPP) reinforced ZK60A magnesium-matrix composites and showed that tensile properties of the composites were reduced by CPP addition, but corrosion resistance enhanced. Lei et al. [14] prepared MMC reinforced by MgO ceramics and Mg–Zn intermetallics which exhibited an enhanced improvement in both mechanical properties and corrosion resistance. Razavi et al. [15]

reported that the addition of Fluorapatite nano particles to magnesium alloy as reinforcement could decrease the corrosion rate. Witte et al. [10] showed that HA particles stabilized the corrosion rate and resulted in a more uniform corrosion attack in artificial sea water and cell solutions. Mensah-Darkwa et al. [25] fabricated Mg-HA composite thin film by means of pulsed laser deposition technique. Their potentiodynamic polarization studies disclosed that the corrosion of Mg plate decreased with an increase of HA ratio in the composite films.

According to the literature using MMC as biomaterial is beneficial due to its adjustable properties which can be achieved by selecting appropriate reinforcement.

Recent investigations have shown that HA particles reinforced magnesium matrix composites would improve the mechanical and electrochemical properties [21, 24]. However, the current manufacturing routes by means of powder metallurgy and conventional casting cause severe particle agglomeration, resulting in to inconsistent performance [1, 11] . Therefore, a route which can prevent sever particle agglomeration could be a promising way to enhance the properties of biodegradable Mg-HA composite. In the present work, the friction stir processing (FSP) was applied to refine Mg structure and fabricate magnesium matrix hydroxyapatite (HA) composite. As is well established, this method is capable of inducing a large degree of plastic deformation to a fairly thick surface layer of the material by mechanical stirring action of a rotating tool and hence, can hinder sever particle agglomeration. Sunil et al. [26] and Ma et al. [27] used FSP to fabricate Mg/HA composite but they did not study the corrosion resistance in details thereby further investigation being required in this area. The present work focuses on the effect of structural modification achieved by FSP as well as the addition of HA on corrosion behaviour of magnesium.

2. Materials and methods

2.1. Materials and workpiece preparation

Workpieces with dimensions of 100×50×8 mm^3 from a commercially pure Mg ingot (holding the purity of 99.8%) were prepared. The workpieces were FSPed using a triangle pin with shoulder diameter of 20 mm, which was machined from H13 tool steel. The workpieces were friction stir processed (FSPed) using 2 passes under predetermined constant rotational (w) and traverse (v) speeds of 1600 rpm and 63 mm/min, respectively [28].

To fabricate Mg-HA composite with 1.5 vol% HA (2.5wt%), a groove with the dimension of 80×1×3 mm^3 was machined on the surface of the FSP workpiece and filled with HA powders (Merck, 2196). HA particles have flake shape with average length of about 100 nm and width of about 20 nm (Fig. 1); these were measured by transmission electron microscopy (TEM, Philips CM12). This was followed by sealing the filled groove using a modified FSP tool that only had a shoulder and no pin to prevent HA particles spreading out during FSP. The workpieces were friction stir processed (FSPed) under predetermined constant rotational and traverse speeds of 1250 rpm and 40 mm/min, respectively.

Fig. 1

2.2. Electrochemical measurements

Dulbecco's phosphate buffered saline (DPBS), with composition of 0.20 g l^{-1} KCl, 0.20 g l^{-1} KH_2PO_4, 8.00 g l^{-1} NaCl and 1.15 g l^{-1} Na_2HPO_4 (anhydrous), 0.1 g l^{-1} $MgCl_2.6H_2O$ and 0.1 g l^{-1}

$CaCl_2$ were used to study the corrosion behaviour. A horizontal three-electrode electrochemical cell with platinum as a counter-electrode, Ag/AgCl (3.5 M KCl, 0,205 vs. SHE/V) as a reference electrode and Mg as a working electrode were chosen. The sample surfaces were ground with SiC abrasive paper up to 1200 grade. The samples with the final surface roughness of Ra=0.1 µm were washed in ethanol under sonication before starting the electrochemical measurements. Single sweep potentiodynamic polarization (PGSTAT302N, Metrohm Autolab B.V.) analysis was performed at 1 mV s^{-1} with initial delay of 20 minutes, between ± 0.4 V versus open circuit potential (OCP).

Electrochemical impedance spectroscopy (EIS) was carried out at OCP (T=37 °C) with initial delay of 20 minutes by applying a sinusoidal wave of 10 mV (peak to peak) amplitude over a frequency range from 10 mHz to 100 kHz for 4 days. OCP was potentiostatically maintained during all measurements. ZSimpwin commercial software (USA) was used to fit the acquired experimental data.

2.3. Microstructural characterization

Standard metallographic procedure including grinding with SiC paper up to 1200 grade, polishing with diamond paste (3 and 1µm) and etching with 12 ml ethanol, 1 ml HNO_3, 3 ml HCl and 4 ml H_2O was applied for further microstructural characterization. Optical microscope (OM, Nikon SMZ 25) and scanning electron microscope (SEM, Phillips XL30) equipped with energy dispersive spectroscopy (EDS) microanalysis were adopted to characterize morphology and composition of the corroded surfaces. Fourier transform infrared (FTIR, Varian 4100) spectroscopy with ATR geometry from 4000 to 500 cm^{-1} was also used to identify the functional

groups in the corrosion products. Texture was measured by X-ray diffractometer (Inel-Equinox 3500, with Mo source, λ=0.709 Å) along with the Nomadic stress system (Cr source, λ=2.2897 Å) and Maud software.

3. Results and discussion

3.1.Microstructure

Microstructure of the sample surfaces are seen in Fig. 2. The initial microstructure of as-cast pure Mg consists of coarse grains (Fig. 2a). On the contrary, as is shown in Fig. 2b, the microstructure of FSPed Mg is characterized by homogenous and refined grains of about 17.7 μm due to the occurrence of dynamic recrystallization [29]. FSP by inducing severe plastic deformation results in breaking the prior structure and creating a large number of low angle grain boundaries and misoriented subgrains as well as favoured places for nucleating recrystallization. The low angle boundaries transform to high angle ones through continues dynamic recrystallization (CDRX). Then, the fine nuclei grow to perfect grains thereby resulting in a fine equiaxed grain microstructure.

The microstructure of Mg-HA composites refined intensely and it is not possible to distinguish the grains by OM (Fig, 2c). The addition of HA particles into the Mg matrix results in finer structure due to the pining grain boundaries and particle stimulate nucleation (PSN) which promote nucleation and prevent grain growth. SEM image of the Mg-HA (Fig. 2d) shows the distribution of HA particles on the surface of Mg. EDS analysis of the marked area in Fig. 2d are listed in Table 1. According to Fig. 2d, the HA powders during FSP as a result of high strain

input have broken and their flake shape changed to spherical like shape with a wide range of diameter (~30 nm to 120 nm).

Fig. 2

Table 1

3.2. Polarization tests

The recorded polarization curves corresponding to 20 minutes after the immersion of as cast, FSPed Mg and Mg-HA composite materials in DPBS solution were plotted in Fig. 3. There is not clear Ecorr shift from as cast neither in FSPed Mg nor in Mg-HA. Break down potential which is due to the rapture of quasi passive film on the surface of samples is observed. Similar passivation behavior for AZ91 magnesium alloy was also reported by Xin [30]. According to the Fig. 3, it is not possible to differentiate between the samples by polarization measurements. Other researchers also reported that polarization is not useful to properly evaluate the corrosion behavior of Mg [31-33]. The polarization curves measure the early stages of corrosion whereas other techniques, which correspond to long-term steady state corrosion behavior, can be more helpful.

Fig. 3

3.3. EIS tests

Fig. 4 shows the impedance modules and phase plots of the samples during immersion in DPBS solution for 96 hours. According to Fig. 4a, the impedance values for the as cast Mg rise at high frequency range while decline at the low frequency range. The Mg-HA composite

demonstrates the same trend during first hours of immersion but by prolonging the immersion time, there is not any sign of decline in impedance values anymore (Fig. 4c). On the contrary, the impedance values of FSPed Mg increased consistently (Fig. 4b). Meanwhile, in the impedance plots of phase angle of as cast Mg (Fig. 4d) during first hours of immersion, one wave trough can be seen at the low frequency range related to inductive behavior, besides two wave crests observed at high and medium frequencies range. Inductive behavior can be also distinguished by decreasing the impedance magnitude (Fig. 4a) at low frequencies ($f<0.1$ Hz). During longer immersion time of as cast Mg, wave crest at middle frequency vanishes. Therefore, the impedance plots of phase angle up to 20 hours of immersion consist of three time constants, namely two capacitance loops and one inductance, whereas there are two time constants (one capacitance and one inductance) at higher immersion times. The Mg-HA (Fig. 4f) composite shows similar behavior to as cast Mg but in this case instead of disappearing medium frequency wave crest, low frequency wave trough disappeared. For FSPed Mg (Fig. 4e), two wave crests appear at high and medium frequency range. It should be noted that although as cast, FSPed and Mg-HA samples have different electrochemical behavior, but impedance values for all of them enhance by increasing the immersion time. However, FSPed Mg revealed significantly higher impedance values over immersion time than that of the others. By disappearing inductive loop in FSPed and Mg-HA, it appears that FSP is able to change the corrosion mechanism.

Fig. 4

The equivalent circuits shown in Fig. 5 used to further elucidating the data and the results are plotted in Fig. 6. To best fit the experimental data, at first, the inductive part which is related to the adsorption of intermediate species were omitted from equivalent circuit; because during experiments it was observed that at low frequency there was not a linear relation between

potential and current. In the second step a constant phase element (CPE), which is often used to describe a non-ideal capacitive behavior, was applied. The impedance of a CPE is introduced by the Eq. 1 [34]:

$$Z = \frac{1}{Q(j\omega)^n} \qquad -1$$

where Z is the CPE impedance (Ω cm^2), Q is admittance (Ω^{-1} cm^{-2} s^n), n is a dimensionless constant ($-1 \leq n \leq 1$), $j = (-1)^{0.5}$, $\omega = 2\pi f$ and f is the frequency [35].

In the equivalent circuits shown in Fig. 5, Rs represents the electrolyte resistance between the working and reference electrode; R_1 is related to both charge transfer and oxide resistance; CPE_1 is the electrochemical double layer capacitance at the substrate/electrolyte interface; CPE_2 introduces the corrosion products capacitance and R_2 has been attributed to pore or ionic conducting defect resistance by some researchers [36, 37]; while the others has related it to corrosion product layer [38-43].

Fig. 5

Fig. 6a exhibits the evolution of R_1 during the immersion time for all the samples. R_1 in as cast Mg increases to about 1100 Ω cm^2 during first 4 hours of immersion; after that reduces and stabilizes around 800 Ω cm^2. The initial increase in the impedance response until 4 h can be related to the formation of a corrosion layer with increasing protective ability over time. Then rapture of the protective layer and localized corrosion happen and decrease the impedance response. Small values of R_2 in as cast Mg (Fig. 6b) demonstrate that the corrosion products on the surface of as cast Mg are not so protective; this can become more porous and soluble by chloride ions attack. As was mentioned above and according to R_2 values in Fig. 6b, after 20 hours of immersion the equivalent circuit with considering just one time constant was chosen for as cast Mg (Fig. 5a). Decreasing the impedance response and the presence of only one capacitive

loop at longer immersion times were attributed to the occurrence of pitting corrosion by Xin et al. [30]. The relative change in impedance response suggests the presence of different corrosion stages in as cast Mg.

FSPed Mg (Fig. 6a), which has the highest R_1 values, exhibits sharp increase in R_1 values during the first hours of immersion. Unlike as cast Mg, R_2 in FSPed Mg increases consistently. These behaviors is in accordance with the formation of more compact corrosion products with enhanced protective ability on the surface of FSPed Mg in comparison to the as cast one. Mg-HA (Figs. 6a and 6b) follows the similar trend as FSPed Mg but the values of R_1 and R_2 are much smaller than those of in FSPed Mg.

According to Figs. 6c and 6d, all the samples have approximately similar Q_1 and n_1 values; while, there is an obvious difference between Q_2 and n_2 values (Figs. 6e and 6f) of the samples. Q_2 values in all samples are much high to consider as faradic phenomena and can be related to corrosion products layer. Mg-HA has lower Q_2 values than FSPed Mg which can be related to the accumulation of corrosion products with different composition or conformation than those on the surface of FSPed Mg. The n_2 values in Mg-HA composite are approximately equal to 0.6 and it is difficult to find any physical explanation for them. According to Fig. 6, in case of pure Mg, R_1 has the most impact on the corrosion resistance. It appears that FSP modifies Mg structure, which hinders charge transfer and improves oxide layer resistance. This suggests more compact and protective corrosion products, while addition of HA eliminates these impacts.

Fig. 6

Based on the OCP values (Fig. 7), FSPed Mg is thermodynamically nobler than Mg-HA composite and the latter is nobler than as cast Mg. The grain refinement achieved through applying FSP on pure Mg results in shifting the OCP towards positive potentials with respect to

the as cast one. The smaller OCP and resistance values of Mg-HA composite than that of FSPed Mg, in spite of smaller grain size in Mg-HA, should be related to interfering other microstructural characteristics that eliminate the impact of grain size; this will be discussed in the following section.

Fig. 7

3.4. Corrosion morphology

OM and SEM images of the corrosion products on the samples immersed in DPBS are seen in Figs. 8 and 9. By comparing the surfaces in Figs. 8a to 8c, it is clear that in as cast Mg there is not any sign of accumulation of corrosion products, while Mg-HA shows the highest accumulation of corrosion products. These results are in agreement with EIS results where R_2 was vanished in as cast Mg. Fig. 9a shows different layers of corrosion products on the surface of as cast Mg including a quasi-adherent sublayer (zone A) and a cracked layer (zone B) due to dehydration. On the surface of FSPed Mg and Mg-HA composite apart from these layers, volcano (Fig. 9b) and needle (Fig. 9c) shape precipitations can be also seen. The hole observed on top of volcano precipitates can be related to the hydrogen gas production during the immersion time; this suggests the presence of cathodic zones underneath the precipitates.

Fig. 8

Fig. 9

To better assess the corrosion attack, the corrosion products were removed and the surfaces were then observed (Fig. 10). It appears that the as cast Mg was suffered from crevice and

filiform and grain boundary attack (Figs. 10a and 10b). The filiform corrosion on magnesium has been already reported by others [31, 43]. Song et al. [44] believed that the corrosion along the grain boundary combined with the pitting corrosion result in typical filiform corrosion in the equal channel angular pressed (ECAPed) samples. According to Fig. 10c, FSPed Mg has corroded a little with small pits without any evidence of filiform corrosion. The grain refinement has likely decreased the galvanic pile between grain boundaries and grain interiors (reduced grain boundary attack) and hence would improve the corrosion resistance with respect to as cast one [45]. Fig. 10d exhibits crevice on the surface of Mg-HA (crevice corrosion was also observed in repeated experiments), which can explain smaller resistance of composite material with respect to FSPed Mg. The un-corroded surface underneath the volcano precipitates on Mg-HA immersed in DPBS (shown by arrows in Fig. 10e) is an evidence that these precipitations have formed on cathodic regions; this was also confirmed by other researchers [34, 46].

Fig. 10

3.5. Corrosion products characterization

Corrosion products formed on the surface of all samples consist of O, C, Ca, P and Mg according to EDS analysis on the selective areas in Fig. 9 (Table 2). It can be seen that volcano and needle precipitates have the same elemental composition as the rest of the corrosion layer. The least value of Ca/P ratio along with the highest value of Oxygen belong to needle like precipitations. Table 2 shows that the values of O and Ca/P ratio increase slightly from inner to outer layer of corrosion products. The value of Ca/P ratio is less than one in this research which can imply to amorphous nature of the products [46]. In addition, the Ca/P ratio can be reduced by

substitution of other ions instead of Ca. The Ca/P ratio in composite materials was higher than that of the others, which can be attributed to the thicker corrosion product layer.

Table 2

The corrosion products were subjected to FTIR analysis to confirm their composition. Fig. 11 reveals similar corrosion products on the surface of all samples. The broad absorption band from 2500 to 3700 cm^{-1} and the band at 1650 cm^{-1} are related to the vibration of water molecules which confirms that the corrosion product layer is indeed hydrated. The peak at 992 cm^{-1} is attributed to phosphate $(PO_4)^{-3}$. The presence of CO_3^{-2} ions is evident by the peaks at 850 and 1454 cm^{-1}. Finally, the peak at 823 cm^{-1} corresponds to the Mg–O bonding vibration [35, 47, 48].

Fig. 11

In this study the significant improvement in corrosion resistance of FSPed Mg with respect to as cast one is attributed to the grain refinement. If the grain size were the only factor determining the corrosion process of Mg, then the Mg-HA sample should have much more corrosion resistance than as cast Mg and FSPed Mg. It appears that the beneficial effects of grain size on corrosion rate is overwhelmed by other microstructural factors, which are induced by FSP.

Crystallographic orientation is one of the important microstructural factors which have impact on corrosion resistance. Different crystallographic planes have different surface energy levels and thus may have various corrosion behaviours. A closely packed plane has a higher binding energy due to its higher atomic coordination and thus lower surface energy. It has been consistently confirmed that the surface with (0 0 0 1) plane has better corrosion resistance with slightly thinner, but more compact film than $(1\ 0\ 1\ \bar{0})$ and $(1\ 1\ 2\ \bar{0})$ planes in spite of the same grain size [49, 50].

The XRD plots and {0004} pole figures of the samples are demonstrated in Fig. 12. According to Fig. 12, as cast Mg exhibits coarse grains with a random texture, while the FSPed one holds basal texture, which may result in better corrosion resistance. Other researchers also observed that in the upper part of FSPed zone, under the influence of the tool shoulder, basal planes were aligned with the tool shoulder surface [51]. Therefore, the fine grain structure and the basal texture together improve the corrosion resistance of FSPed Mg with respect to as cast one. In comparison, the texture intensity has been decreased by HA particles addition to Mg. This texture reduction is due to the presence of HA particles, which stimulate the recrystallization of randomly-oriented grains by particle stimulation nucleation (PSN) mechanism. In the research performed by Garcés et al. [52], the texture of Mg matrix was also vanished by reinforcement particles. In addition, Campo et al. [24] found that the reinforcement particles tend to prevent the appearance of the texture produced by the extrusion process.

Fig. 12

4. Discussion

The following reactions can be happened (reactions 1 to 7) where Mg immersed in DPBS:

$$Mg \rightarrow Mg^{+} + e^{-} \quad -1$$

$$Mg^{+} + H_2O \rightarrow Mg^{2+} + OH^{-} + \frac{1}{2}H_2 \quad -2$$

The anodic hydrogen evolution is only special feature for magnesium alloys which has been known as negative difference effect (NDE) [53, 54].

$$H_2O + e^{-} \rightarrow OH^{-} + \frac{1}{2}H_2 \quad -3$$

$$H_2PO_4^- + 2OH^- \rightarrow PO_4^{3-} + 2H_2O \quad -4$$

$$2HPO_4^{2-} + 2OH^- \rightarrow 2PO_4^{3-} + 2H_2O \quad -5$$

$$Mg + 2H_2O \rightarrow Mg(OH)_2 + H_2 \quad -6$$

$$Mg^{2+} + Ca^{2+} + PO_4^{3-} \rightarrow Ca_3Mg_3(PO_4)_4 \quad -7$$

The evolution of the corrosion behaviour over immersion time is referred to the accumulation of magnesium hydroxide and calcium phosphate base precipitations according to reactions 6 and 7. These form mixed layers that hinder the reaction of chloride and any atomic-ionic movement through the corrosion products layer. Diminishing the R_2 in as cast Mg over time indicates that the mix layers on as cast Mg surface are not as protective as ones on FSPed Mg or Mg-HA composite. Disappearance of the R_2 after about 20 h can be assigned to the heavy damage in the protective surface film induced by chlorides. Aggressive Cl^- species in the solution accelerate the dissolution/rupture of the corrosion layer, initiate localized corrosion process and pit formation. This is followed by lateral pits growing as a result of self-limiting feature of Mg [55]. Meanwhile, the simultaneous formation of a porous $Mg(OH)_2$ and calcium phosphate base products inside the pit cavity is occurred.

The results demonstrate that the refined microstructure, which is induced by FSP, improves the corrosion resistance of Mg. The rapid formation of oxide film, higher interfacial adherence of oxide film at grain boundaries and the reduction of galvanic couple intensity between grain interior and grain boundaries are probably the reasons for better corrosion resistance of fine grained Mg [45, 56, 57]. Moreover, Kim and Kim [58] distinguished isolated MgO nanocrystals on the fine-grained Mg substrate under the MgO layer which can reduce cracking susceptibility

of the MgO layer or the interface between MgO and the Mg substrate by decreasing the sharpness of the tensile stress gradient across the interface. In addition, the dissolution of impurities at the grain boundaries can be promoted by decreasing the grain size thereby reducing the cathodic sites for cathodic reaction [59, 60]. Furthermore, FSP dominated basal texture would cooperate with grain refinement to increase the corrosion resistance of FSPed Mg.

In Mg-HA composite, the protective mixed layer was more easily generated on the surface since HA particles can act as the nucleation sites. Ning and Zhou [61] also reported that HA-Ti composite fabricated by the powder metallurgy technique could induce apatite nucleation and growth on its surface in simulated body fluid (SBF). Although, the accumulation of corrosion products in case of Mg-HA is much higher than the others, these products based on the obtained results appear porous and they cannot prevent corrosion efficiently.

Razavi et al. [62] believed that large amounts of magnesium ion released during corrosion of the AZ91 Mg alloy would possibly inactivate apatite formation thereby resulting in less apatite formation around the AZ91 sample if compared to the composite magnesium–fluorapatite (FA). Hence, according to their hypothesis, the higher accumulation of corrosion products was attributed to the less corrosion rate of composite material. In addition, the amount of direct contact with SBF solution is reduced in Mg-FA composite which enhances corrosion resistance more. However, in this study, their hypothesis cannot be supported by comparing corrosion resistance of FSPed Mg and Mg-HA. The Mg-HA composite demonstrates higher accumulation of corrosion products but lower corrosion resistance than FSPed Mg. Probably, the higher thickness of corrosion layer and the presence of HA particles has induced the stresses. This may also result in the subsequent cracking of those layers thereby providing the accessibility of water and chloride ions towards the Mg substrate and continuation of corrosion process.

Moreover, HA reinforcements create preferential locations for corrosion attacks due to the presence of Mg matrix/HA interface and breaking the continuity of the Mg matrix. The corrosion reactions proceed rapidly through the Mg matrix and HA particles interface as is shown in Fig. 13. Similar enhanced corrosion rate of composites was also found by Gu et al. [11] and Pardo et al. [63]. Apart from these results, embedding HA particles in Mg matrix has reduced the basal texture intensity and hence, deteriorated the corrosion resistance with respect to FSPed Mg.

Fig. 13

These observations together with the current results indicate that the corrosion performance of Mg is determined by competition between grain size and texture. Decreasing the crevice susceptibility in FSPed Mg with respect to the others can disclose that the corrosion mechanism can be changed by modifying the Mg microstructure.

5. Conclusion

The corrosion behavior of as cast Mg, FSPed Mg and Mg-HA composite was evaluated in Dulbecco's phosphate buffered saline (DPBS) solution up to 96 h and the following conclusions were drawn.

1. Friction stir processing can increase the corrosion resistance of pure Mg by decreasing the grain size and dominating basal texture.

2. Modifying the Mg microstructure by FSP would change the corrosion mechanism of pure Mg. This results in formation of more compact corrosion product layers, which hinder the

aggressive role of chloride ions. Significant increase in corrosion resistance of FSPed Mg can be related to its less crevice susceptibility than the others.

3. Corrosion performance of Mg is determined by competition between grain size and texture. Although Mg-HA composite possesses the finest grain size, the HA particles reduce the basal texture intensity and probably break the continuity of the Mg matrix which have detrimental effect on corrosion resistance of Mg.

References

[1] A. Feng, Y. Han, Mechanical and in vitro degradation behavior of ultrafine calcium polyphosphate reinforced magnesium-alloy composites, Materials & Design, 32 (2011) 2813-2820.

[2] E. Zhang, L. Yang, J. Xu, H. Chen, Microstructure, mechanical properties and bio-corrosion properties of Mg–Si (–Ca, Zn) alloy for biomedical application, Acta biomaterialia, 6 (2010) 1756-1762.

[3] F. Witte, The history of biodegradable magnesium implants: a review, Acta Biomaterialia, 6 (2010) 1680-1692.

[4] A.C. Hänzi, I. Gerber, M. Schinhammer, J.F. Löffler, P.J. Uggowitzer, On the in vitro and in vivo degradation performance and biological response of new biodegradable Mg–Y–Zn alloys, Acta biomaterialia, 6 (2010) 1824-1833.

[5] Y. Zong, G. Yuan, X. Zhang, L. Mao, J. Niu, W. Ding, Comparison of biodegradable behaviors of AZ31 and Mg–Nd–Zn–Zr alloys in Hank's physiological solution, Materials Science and Engineering: B, 177 (2012) 395-401.

[6] N.I.Z. Abidin, B. Rolfe, H. Owen, J. Malisano, D. Martin, J. Hofstetter, P.J. Uggowitzer, A. Atrens, The in vivo and in vitro corrosion of high-purity magnesium and magnesium alloys WZ21 and AZ91, Corrosion Science, 75 (2013) 354-366.

[7] H. Hornberger, S. Virtanen, A. Boccaccini, Biomedical coatings on magnesium alloys–a review, Acta biomaterialia, 8 (2012) 2442-2455.

[8] L. Li, J. Gao, Y. Wang, Evaluation of cyto-toxicity and corrosion behavior of alkali-heat-treated magnesium in simulated body fluid, Surface and Coatings Technology, 185 (2004) 92-98.

[9] Y. Wang, M. Wei, J. Gao, Improve corrosion resistance of magnesium in simulated body fluid by dicalcium phosphate dihydrate coating, Materials Science and Engineering: C, 29 (2009) 1311-1316.

[10] F. Witte, F. Feyerabend, P. Maier, J. Fischer, M. Störmer, C. Blawert, W. Dietzel, N. Hort, Biodegradable magnesium–hydroxyapatite metal matrix composites, Biomaterials, 28 (2007) 2163-2174.

[11] X. Gu, W. Zhou, Y. Zheng, L. Dong, Y. Xi, D. Chai, Microstructure, mechanical property, bio-corrosion and cytotoxicity evaluations of Mg/HA composites, Materials Science and Engineering: C, 30 (2010) 827-832.

[12] K.A. Khalil, A.A. Almajid, Effect of high-frequency induction heat sintering conditions on the microstructure and mechanical properties of nanostructured magnesium/hydroxyapatite nanocomposites, Materials & Design, 36 (2012) 58-68.

[13] A. Feng, Y. Han, The microstructure, mechanical and corrosion properties of calcium polyphosphate reinforced ZK60A magnesium alloy composites, Journal of Alloys and Compounds, 504 (2010) 585-593.

[14] T. Lei, W. Tang, S.H. Cai, F.F. Feng, N.F. Li, On the corrosion behaviour of newly developed biodegradable Mg-based metal matrix composites produced by in situ reaction, Corrosion Science, 54 (2012) 270-277.

[15] M. Razavi, M. Fathi, M. Meratian, Bio-corrosion behavior of magnesium-fluorapatite nanocomposite for biomedical applications, Materials Letters, 64 (2010) 2487-2490.

[16] D.B. Liu, Y. Huang, P. Prangnell, Microstructure and performance of a biodegradable Mg–1Ca–2Zn–1TCP composite fabricated by combined solidification and deformation processing, Materials Letters, 82 (2012) 7-9.

[17] X. Wang, P. Zhang, L. Dong, X. Ma, J. Li, Y. Zheng, Microstructure and characteristics of interpenetrating β-TCP/Mg–Zn–Mn composite fabricated by suction casting, Materials & Design, 54 (2014) 995-1001.

[18] D. Liu, Y. Zuo, W. Meng, M. Chen, Z. Fan, Fabrication of biodegradable nano-sized β-TCP/Mg composite by a novel melt shearing technology, Materials Science and Engineering: C, 32 (2012) 1253-1258.

[19] Y. Zheng, X. Gu, Y. Xi, D. Chai, In vitro degradation and cytotoxicity of Mg/Ca composites produced by powder metallurgy, Acta biomaterialia, 6 (2010) 1783-1791.

[20] K. Yu, L. Chen, J. Zhao, S. Li, Y. Dai, Q. Huang, Z. Yu, In vitro corrosion behavior and in vivo biodegradation of biomedical β-Ca 3 (PO 4) 2/Mg–Zn composites, Acta biomaterialia, 8 (2012) 2845-2855.

[21] B.R. Sunil, C. Ganapathy, T.S. Kumar, U. Chakkingal, Processing and mechanical behavior of lamellar structured degradable magnesium–hydroxyapatite implants, Journal of the mechanical behavior of biomedical materials, 40 (2014) 178-189.

[22] X. Gu, X. Wang, N. Li, L. Li, Y. Zheng, X. Miao, Microstructure and characteristics of the metal–ceramic composite (MgCa-HA/TCP) fabricated by liquid metal infiltration, Journal of Biomedical Materials Research Part B: Applied Biomaterials, 99 (2011) 127-134.

[23] X. Ye, M. Chen, M. Yang, J. Wei, D. Liu, In vitro corrosion resistance and cytocompatibility of nano-hydroxyapatite reinforced Mg–Zn–Zr composites, Journal of Materials Science: Materials in Medicine, 21 (2010) 1321-1328.

[24] R. del Campo, B. Savoini, A. Muñoz, M. Monge, G. Garcés, Mechanical properties and corrosion behavior of Mg–HAP composites, Journal of the mechanical behavior of biomedical materials, 39 (2014) 238-246.

[25] K. Mensah Darkwa, R.K. Gupta, D. Kumar, Mechanical and Corrosion Properties of Magnesium-Hydroxyapatite (Mg-HA) Composite Thin Films, Journal of Materials Science and Technology, 29 (2013) 788-794.

[26] B.R. Sunil, T.S. Kumar, U. Chakkingal, V. Nandakumar, M. Doble, Friction stir processing of magnesium–nanohydroxyapatite composites with controlled in vitro degradation behavior, Materials Science and Engineering: C, 39 (2014) 315-324.

[27] C. Ma, L. Chen, J. Xu, A. Fehrenbacher, Y. Li, F.E. Pfefferkorn, N.A. Duffie, J. Zheng, X. Li, Effect of fabrication and processing technology on the biodegradability of magnesium nanocomposites, Journal of Biomedical Materials Research Part B: Applied Biomaterials, 101 (2013) 870-877.

[28] D. Ahmadkhaniha, M. Heydarzadeh Sohi, A. Zarei-Hanzaki, S.M. Bayazid, M. Saba. Taguchi optimization of process parameters in friction stir processing of pure Mg, Journal of Magnesium and Alloys, In press.

[29] R.S. Mishra, Z. Ma, Friction stir welding and processing, Materials Science and Engineering: R: Reports, 50 (2005) 1-78.

[30] Y. Xin, C. Liu, X. Zhang, G. Tang, X. Tian, P.K. Chu, Corrosion behavior of biomedical AZ91 magnesium alloy in simulated body fluids, Journal of Materials Research, 22 (2007) 2004-2011.

[31] E. Mostaed, M. Hashempour, A. Fabrizi, D. Dellasega, M. Bestetti, F. Bonollo, M. Vedani, Microstructure, texture evolution, mechanical properties and corrosion behavior of ECAP processed ZK60 magnesium alloy for biodegradable applications, journal of the mechanical behavior of biomedical materials, 37 (2014) 307-322.

[32] Z. Shi, M. Liu, A. Atrens, Measurement of the corrosion rate of magnesium alloys using Tafel extrapolation, Corrosion science, 52 (2010) 579-588.

[33] G. Song, A. Atrens, Understanding magnesium corrosion—a framework for improved alloy performance, Advanced engineering materials, 5 (2003) 837-858.

[34] M. Ascencio, M. Pekguleryuz, S. Omanovic, An investigation of the corrosion mechanisms of WE43 Mg alloy in a modified simulated body fluid solution: The influence of immersion time, Corrosion Science, 87 (2014) 489-503.

[35] M. Ascencio, M. Pekguleryuz, S. Omanovic, An investigation of the corrosion mechanisms of WE43Mg alloy in a modified simulated body fluid solution: The effect of electrolyte renewal, Corrosion Science, 91 (2015) 297-310.

[36] Y. Xin, T. Hu, P.K. Chu, Degradation behaviour of pure magnesium in simulated body fluids with different concentrations of, Corrosion Science, 53 (2011) 1522-1528.

[37] X.W. Guo, J.W. Chang, S.M. He, W.J. Ding, X. Wang, Investigation of corrosion behaviors of Mg–6Gd–3Y–0.4 Zr alloy in NaCl aqueous solutions, Electrochimica Acta, 52 (2007) 2570-2579.

[38] S. Zhang, J. Li, Y. Song, C. Zhao, X. Zhang, C. Xie, Y. Zhang, H. Tao, Y. He, Y. Jiang, In vitro degradation, hemolysis and MC3T3-E1 cell adhesion of biodegradable Mg–Zn alloy, Materials Science and Engineering: C, 29 (2009) 1907-1912.

[39] N.D. Nam, M. Mathesh, M. Forsyth, D.S. Jo, Effect of manganese additions on the corrosion behavior of an extruded Mg–5Al based alloy, Journal of Alloys and Compounds, 542 (2012) 199-206.

[40] N. Kirkland, N. Birbilis, M. Staiger, Assessing the corrosion of biodegradable magnesium implants: a critical review of current methodologies and their limitations, Acta biomaterialia, 8 (2012) 925-936.

[41] G.L. Song, Z. Xu, Crystal orientation and electrochemical corrosion of polycrystalline Mg, Corrosion Science, 63 (2012) 100-112.

[42] Y. Song, E.H. Han, K. Dong, D. Shan, C.D. Yim, B.S. You, Study of the corrosion product films formed on the surface of Mg–xZn alloys in NaCl solution, Corrosion Science, 88 (2014) 215-225.

[43] A. Samaniego, I. Llorente, S. Feliu, Combined effect of composition and surface condition on corrosion behaviour of magnesium alloys AZ31 and AZ61, Corrosion Science, 68 (2013) 66-71.

[44] D. Song, A. Ma, J. Jiang, P. Lin, D. Yang, J. Fan, Corrosion behaviour of bulk ultra-fine grained AZ91D magnesium alloy fabricated by equal-channel angular pressing, Corrosion Science, 53 (2011) 362-373.

[45] G. Argade, S. Panigrahi, R. Mishra, Effects of grain size on the corrosion resistance of wrought magnesium alloys containing neodymium, Corrosion Science, 58 (2012) 145-151.

[46] R. Rettig, S. Virtanen, Composition of corrosion layers on a magnesium rare-earth alloy in simulated body fluids, Journal of Biomedical Materials Research Part A, 88 (2009) 359-369.

[47] M.I. Jamesh, G. Wu, Y. Zhao, D.R. McKenzie, M.M. Bilek, P.K. Chu, Electrochemical corrosion behavior of biodegradable Mg–Y–RE and Mg–Zn–Zr alloys in Ringer's solution and simulated body fluid, Corrosion Science, 91 (2015) 160-184.

[48] M. Jamesh, S. Kumar, T.S. Narayanan, Corrosion behavior of commercially pure Mg and ZM21 Mg alloy in Ringer's solution–Long term evaluation by EIS, Corrosion Science, 53 (2011) 645-654.

[49] G.L. Song, Z. Xu, Effect of microstructure evolution on corrosion of different crystal surfaces of AZ31 Mg alloy in a chloride containing solution, Corrosion Science, 54 (2012) 97-105.

[50] R. Xin, Y. Luo, A. Zuo, J. Gao, Q. Liu, Texture effect on corrosion behavior of AZ31 Mg alloy in simulated physiological environment, Materials Letters, 72 (2012) 1-4.

[51] S.H.C. Park, Y.S. Sato, H. Kokawa, Basal plane texture and flow pattern in friction stir weld of a magnesium alloy, Metallurgical and Materials Transactions A, 34 (2003) 987-994.

[52] G. Garcés, M. Rodríguez, P. Pérez, P. Adeva, High temperature mechanical properties of Mg–Y 2 O 3 composite: Competition between texture and reinforcement contributions, Composites science and technology, 67 (2007) 632-637.

[53] A. King, N. Birbilis, J. Scully, Accurate electrochemical measurement of magnesium corrosion rates; a combined impedance, mass-loss and hydrogen collection study, Electrochimica Acta, 121 (2014) 394-406.

[54] G. Song, A. Atrens, D. Stjohn, J. Nairn, Y. Li, The electrochemical corrosion of pure magnesium in 1 N NaCl, Corrosion Science, 39 (1997) 855-875.

[55] M.C. Zhao, M. Liu, G.L. Song, A. Atrens, Influence of pH and chloride ion concentration on the corrosion of Mg alloy ZE41, Corrosion Science, 50 (2008) 3168-3178.

[56] K. Ralston, N. Birbilis, Effect of grain size on corrosion: a review, Corrosion, 66 (2010) 075005-075005-075013.

[57] G. Argade, K. Kandasamy, S. Panigrahi, R. Mishra, Corrosion behavior of a friction stir processed rare-earth added magnesium alloy, Corrosion Science, 58 (2012) 321-326.

[58] H. Kim, W. Kim, Enhanced corrosion resistance of ultrafine-grained AZ61 alloy containing very fine particles of Mg 17 Al 12 phase, Corrosion Science, 75 (2013) 228-238.

[59] Z. Pu, G.L. Song, S. Yang, J. Outeiro, O. Dillon, D. Puleo, I. Jawahir, Grain refined and basal textured surface produced by burnishing for improved corrosion performance of AZ31B Mg alloy, Corrosion Science, 57 (2012) 192-201.

[60] Z. Pu, S. Yang, G.L. Song, O. Dillon, D. Puleo, I. Jawahir, Ultrafine-grained surface layer on Mg–Al–Zn alloy produced by cryogenic burnishing for enhanced corrosion resistance, Scripta Materialia, 65 (2011) 520-523.

[61] C. Ning, Y. Zhou, In vitro bioactivity of a biocomposite fabricated from HA and Ti powders by powder metallurgy method, Biomaterials, 23 (2002) 2909-2915.

[62] M. Razavi, M. Fathi, M. Meratian, Fabrication and characterization of magnesium–fluorapatite nanocomposite for biomedical applications, Materials Characterization, 61 (2010) 1363-1370.

[63] A. Pardo, S. Merino, M. Merino, I. Barroso, M. Mohedano, R. Arrabal, F. Viejo, Corrosion behaviour of silicon–carbide-particle reinforced AZ92 magnesium alloy, Corrosion Science, 51 (2009) 841-849.

Figure captions

Fig. 1. TEM image of HA particles.

Fig. 2. OM images of (a) as cast Mg, (b) FSPed Mg, (c) Mg-HA composite, (d) SEM image of Mg-HA composite.

Fig. 3. Polarization plots of different samples in DPBS solutions.

Fig. 4. Impedance modules and phase plots of the samples immersed in DPBS for 96 hours (a, d) as cast Mg, OCP values changed from -1.78 to -1.75 v during immersion time (b, e) FSPed Mg, OCP values changed from -1.63 to -1.60 v during immersion time (c, f) Mg-HA, OCP values changed from -1.76 to -1.72 v during immersion time.

Fig. 5. Equivalent circuit used for fitting the data of (a) as cast Mg after 20 h of immersion, (b) other conditions.

Fig. 6. Fitting data versus immersion time for as cast Mg, FSPed Mg and Mg-HA.

Fig. 7. OCP values of the samples versus immersion time.

Fig. 8. Optical images of corroded surfaces of (a) as cast Mg, (b) FSPed Mg, (c) Mg-HA.

Fig. 9. SEM images of corroded surfaces (a) as cast Mg, (b) volcano like precipitation, (c) needle like precipitations on the surface of processed Mg.

Fig. 10. SEM images of the corroded surfaces after removing the corrosion products (a, b) as cast, (c) FSPed Mg, (d) Mg-HA, (e) OM image of Mg-HA corroded surface after removing the corrosion products.

Fig. 11. FTIR analysis of the corrosion products on the surface of the samples immersed in DPBS solution.

Fig. 12. Pole figures and XRD plots of (a) as cast Mg, (b) FSPed Mg, (c) Mg-HA.

Fig. 13. Corroded surface of Mg-HA composite.

Table 1
EDS analysis of Zone A and B in Fig. 2d

Elements		O	Mg	P	Ca	Au
Zone A	At%	13.78	82.25	1.29	1.60	1.08
Zone B	At%	5.04	94.05	0	0	0.9

Table 2

EDS analysis of the corrosion products on the surface of samples immersed in DPBS

Elements (At%)	C	O	Na	Mg	P	Cl	K	Ca	Ca/P
Zone A	13.16	58.30	0.91	11.01	9.04	0.83	0.13	6.62	0.73
Zone B	13.05	59	0.90	9.60	9.47	0.73	0.12	7.13	0.75
Zone C	11.54	63.42	2.33	5.27	9.10	0.51	0.35	7.48	0.82
Zone D	8.02	72.13	3.68	6.46	6.10	0.29	1.71	1.61	0.26

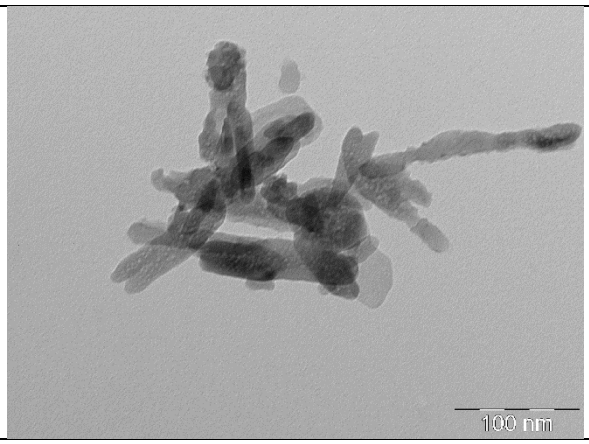

Fig. 1. TEM image of HA particles.

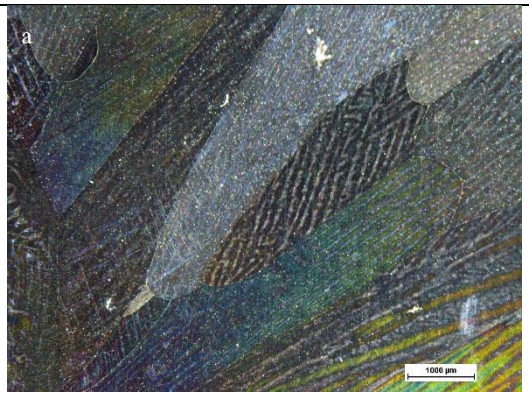

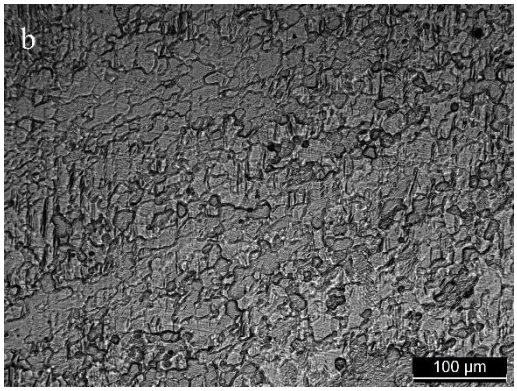

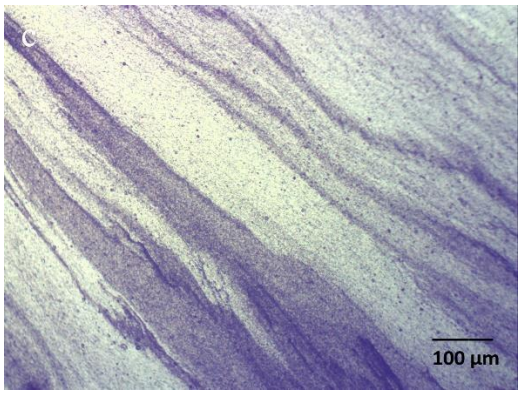

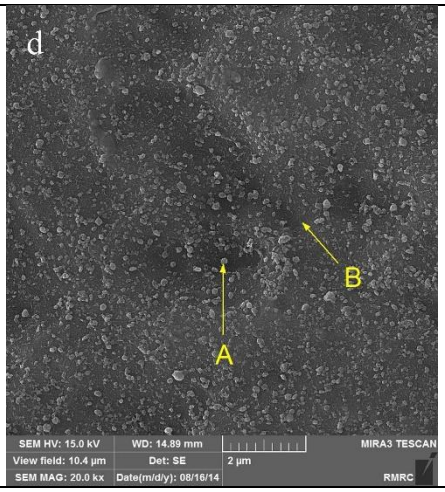

Fig. 2. OM images of (a) as cast Mg, (b) FSPed Mg, (c) Mg-HA composite, (d) SEM image of Mg-HA composite.

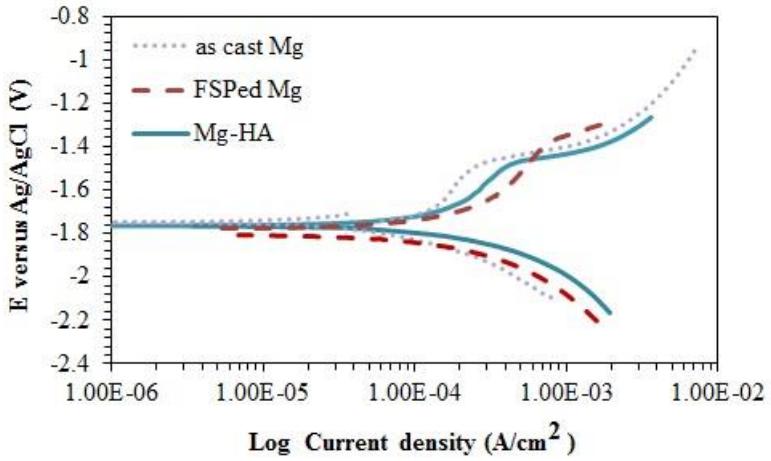

Fig. 3. Polarization plots of different samples in DPBS solutions.

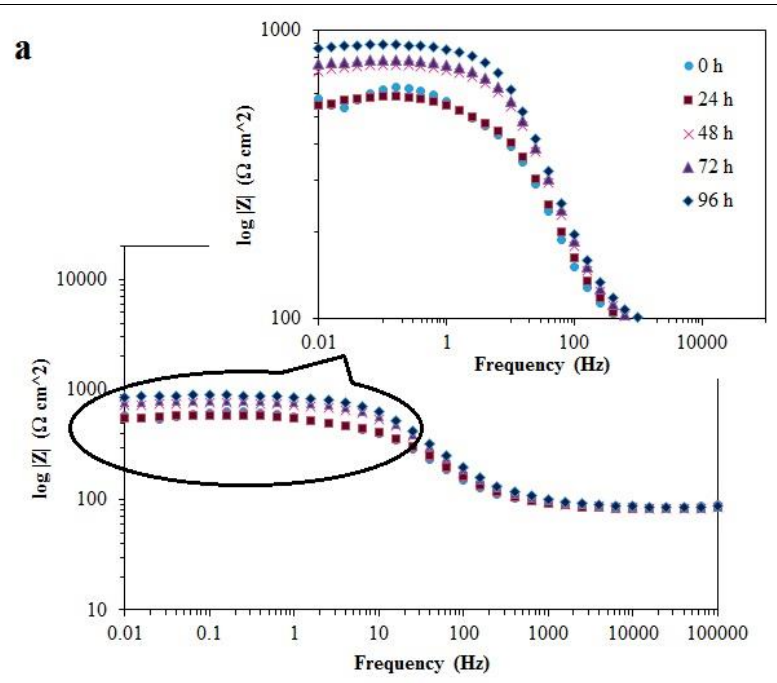

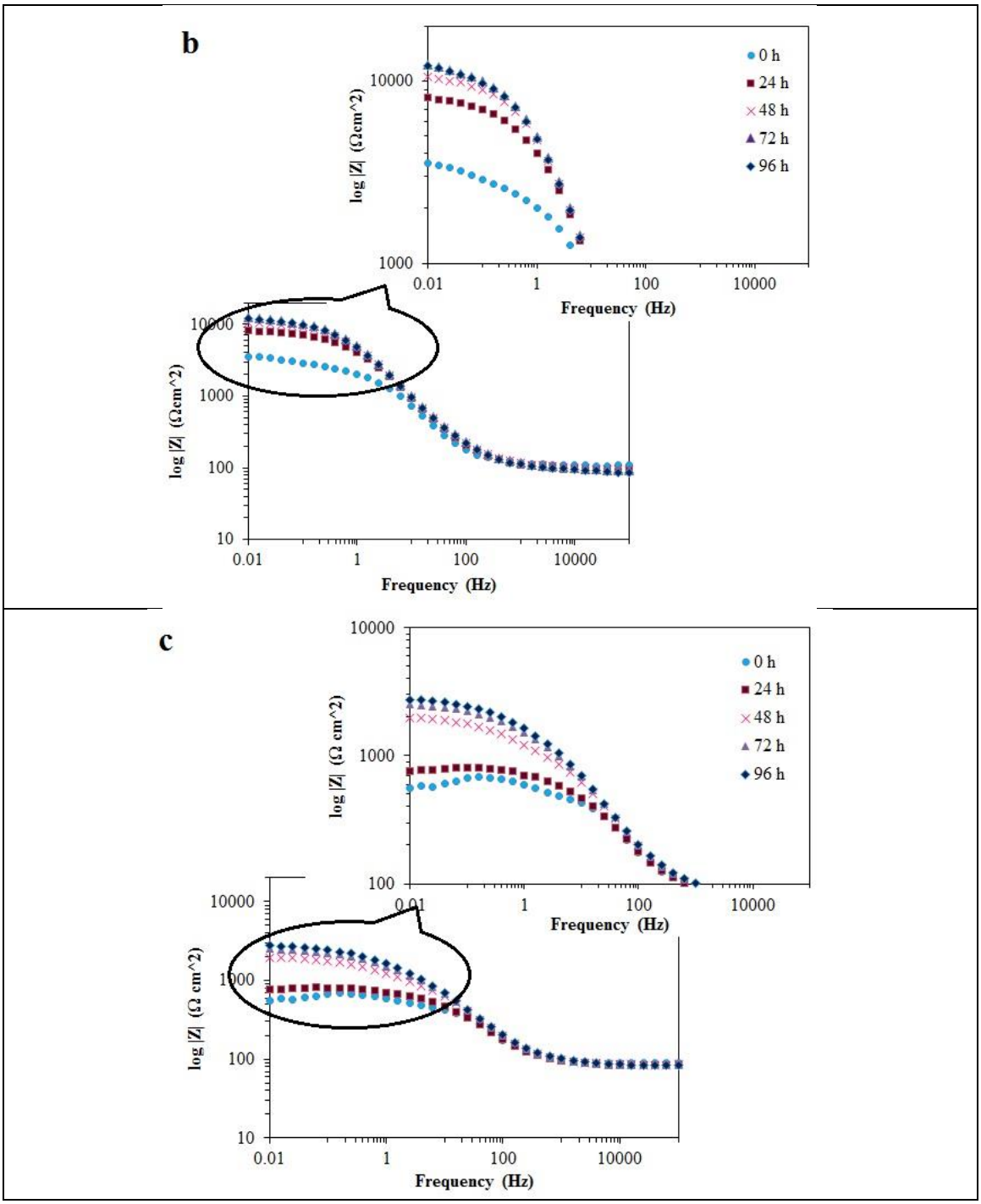
b
0 h
24 h
48 h
72 h
96 h
log |Z| (Ωcm^2)
Frequency (Hz)
c
log |Z| (Ω cm^2)
Frequency (Hz)

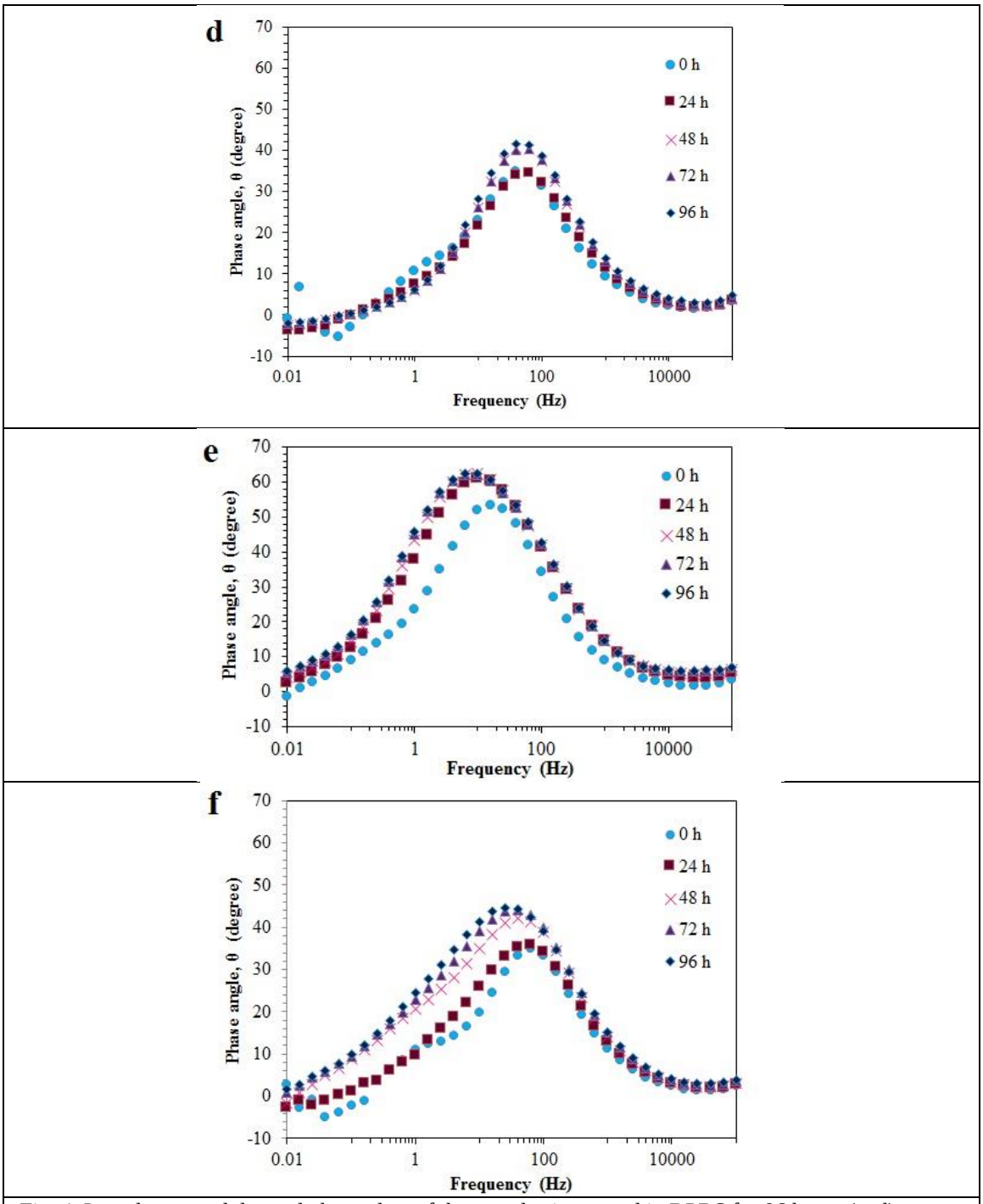

Fig. 4. Impedance modules and phase plots of the samples immersed in DPBS for 96 hours (a, d) as cast Mg, OCP values changed from -1.78 to -1.75 v during immersion time (b, e) FSPed Mg, OCP values changed from -1.63 to -1.60 v during immersion time (c, f) Mg-HA, OCP values changed from -1.76 to -1.72 v during immersion time.

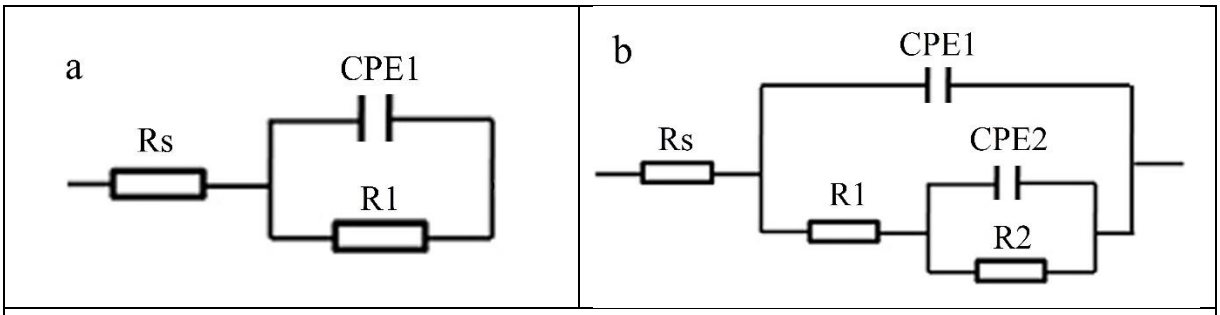

Fig. 5. Equivalent circuit used for fitting the data of (a) as cast Mg after 20 h of immersion, (b) other conditions.

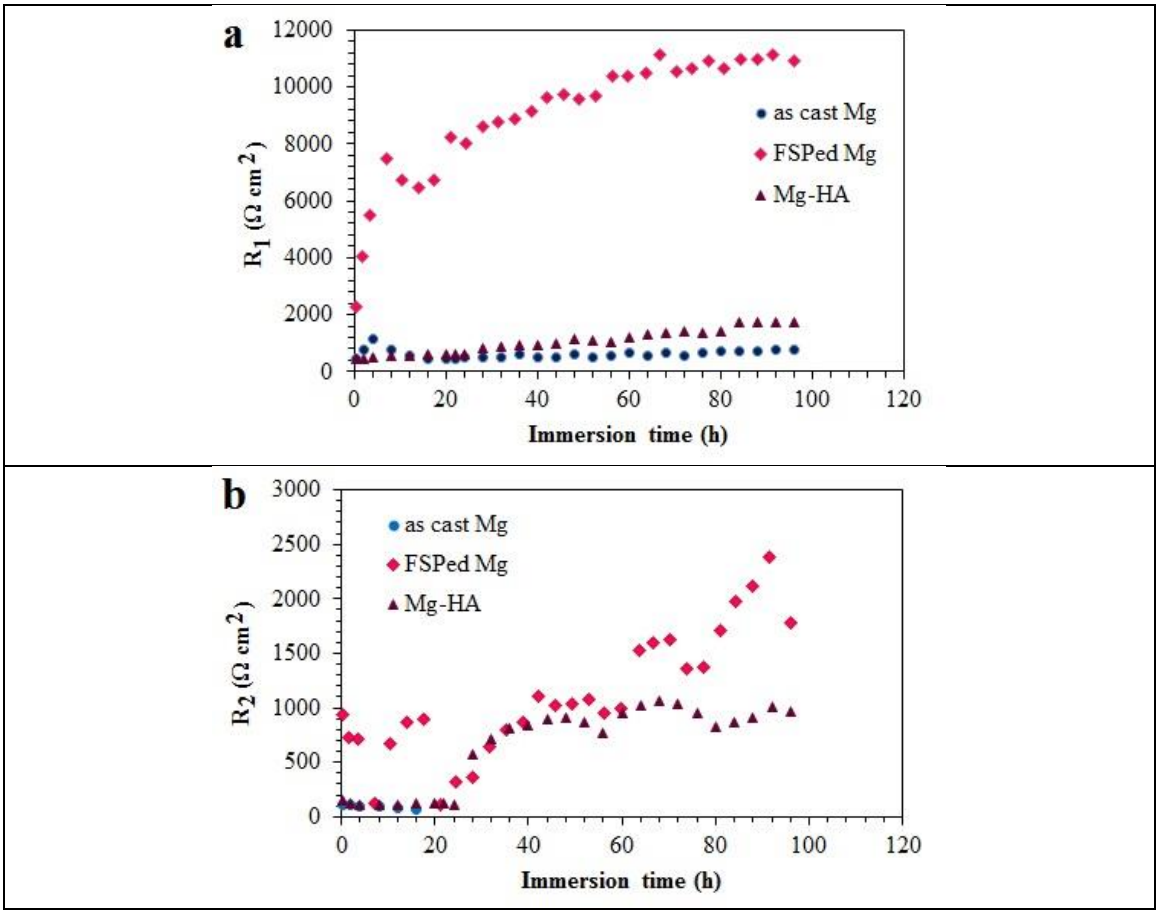

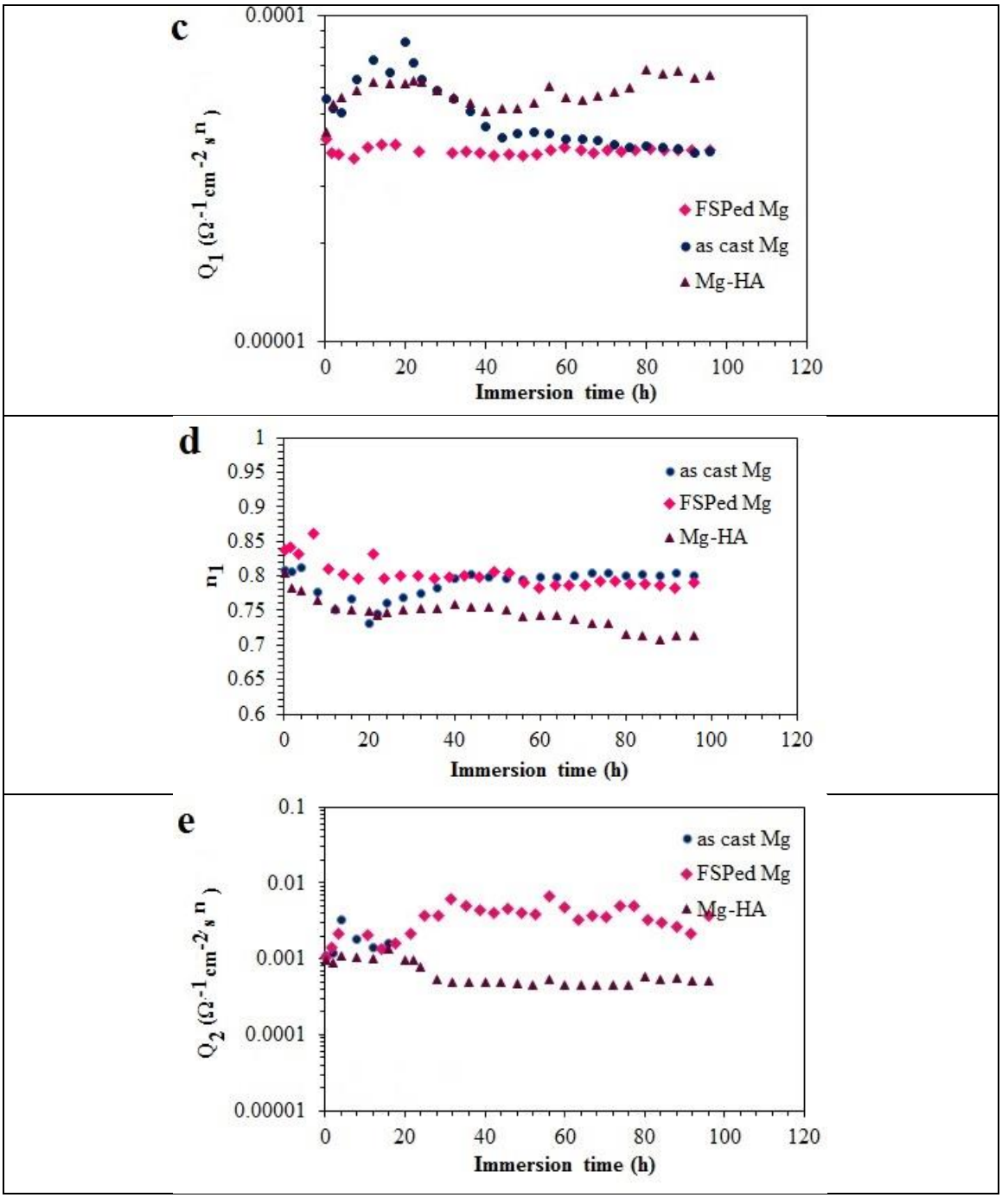
c
0.0001
0.00001
Q_1 ($\Omega^{-1}cm^{-2}s^n$)
FSPed Mg
as cast Mg
Mg-HA
0
20
40
60
80
100
120
Immersion time (h)
d
1
0.95
0.9
0.85
0.8
0.75
0.7
0.65
0.6
n_1
as cast Mg
FSPed Mg
Mg-HA
Immersion time (h)
e
0.1
0.01
0.001
0.0001
0.00001
Q_2 ($\Omega^{-1}cm^{-2}s^n$)
as cast Mg
FSPed Mg
Mg-HA
Immersion time (h)

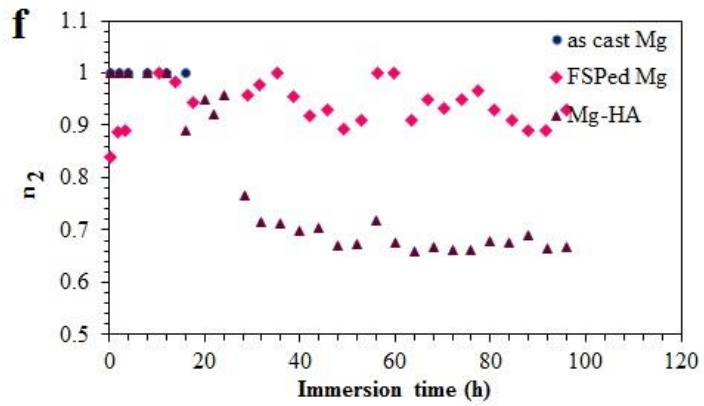

Fig. 6. Fitting data versus immersion time for as cast Mg, FSPed Mg and Mg-HA.

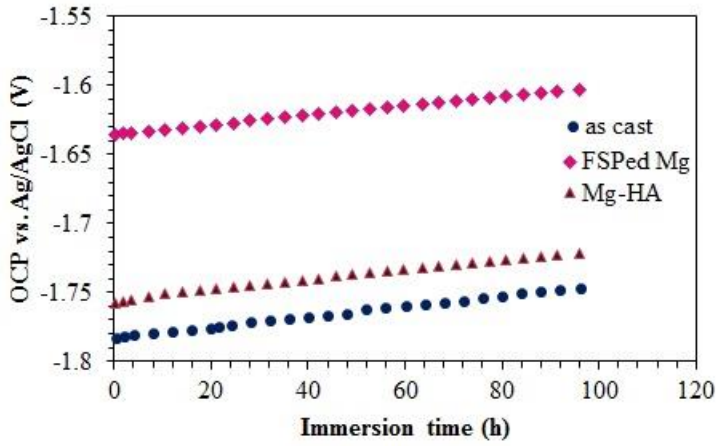

Fig. 7. OCP values of the samples versus immersion time.

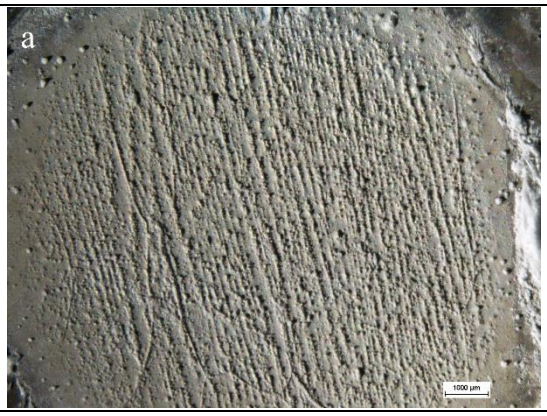

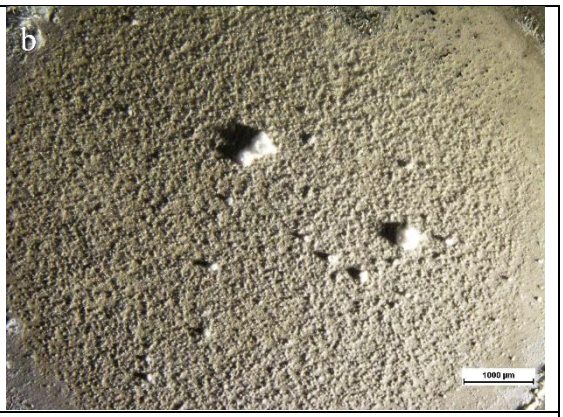

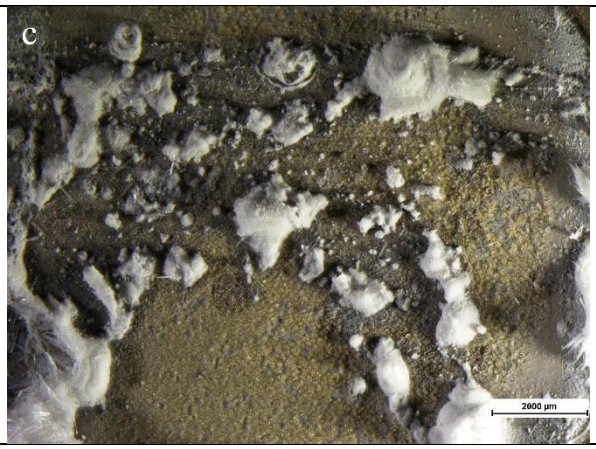

Fig. 8. Optical images of corroded surfaces of (a) as cast Mg, (b) FSPed Mg, (c) Mg-HA.

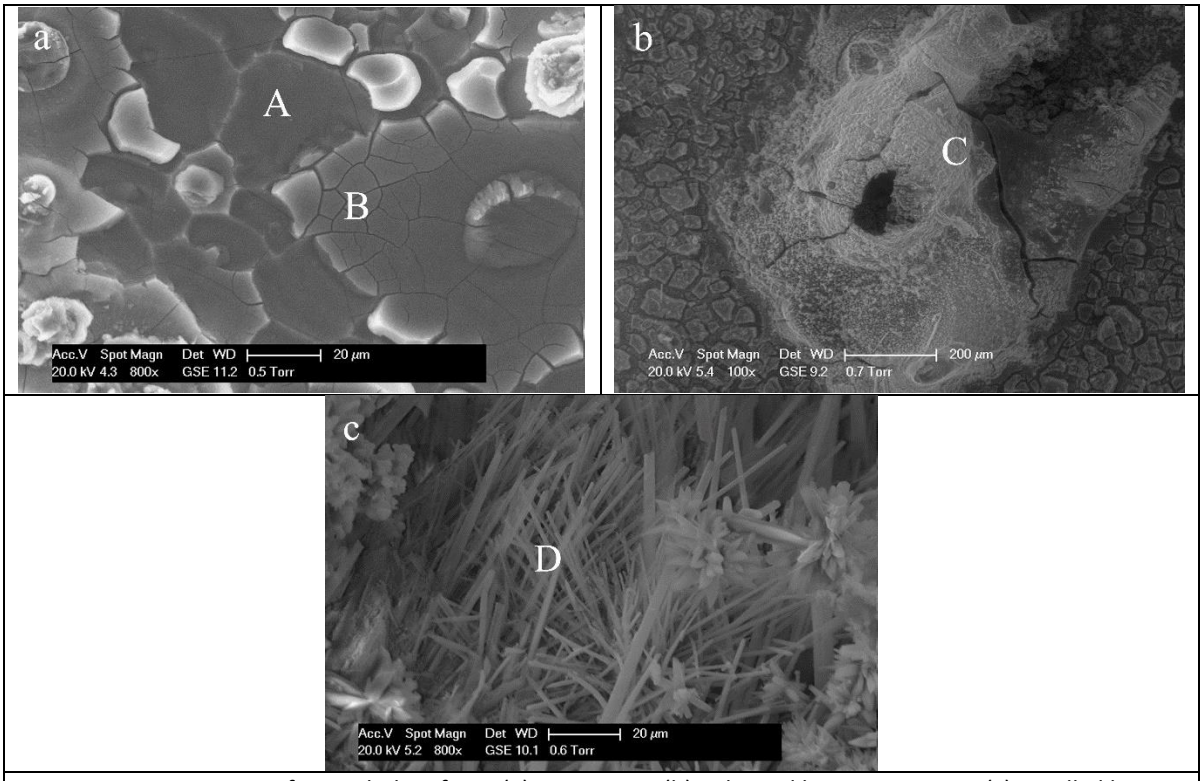

Fig. 9. SEM images of corroded surfaces (a) as cast Mg, (b) volcano like precipitation, (c) needle like precipitations on the surface of processed Mg.

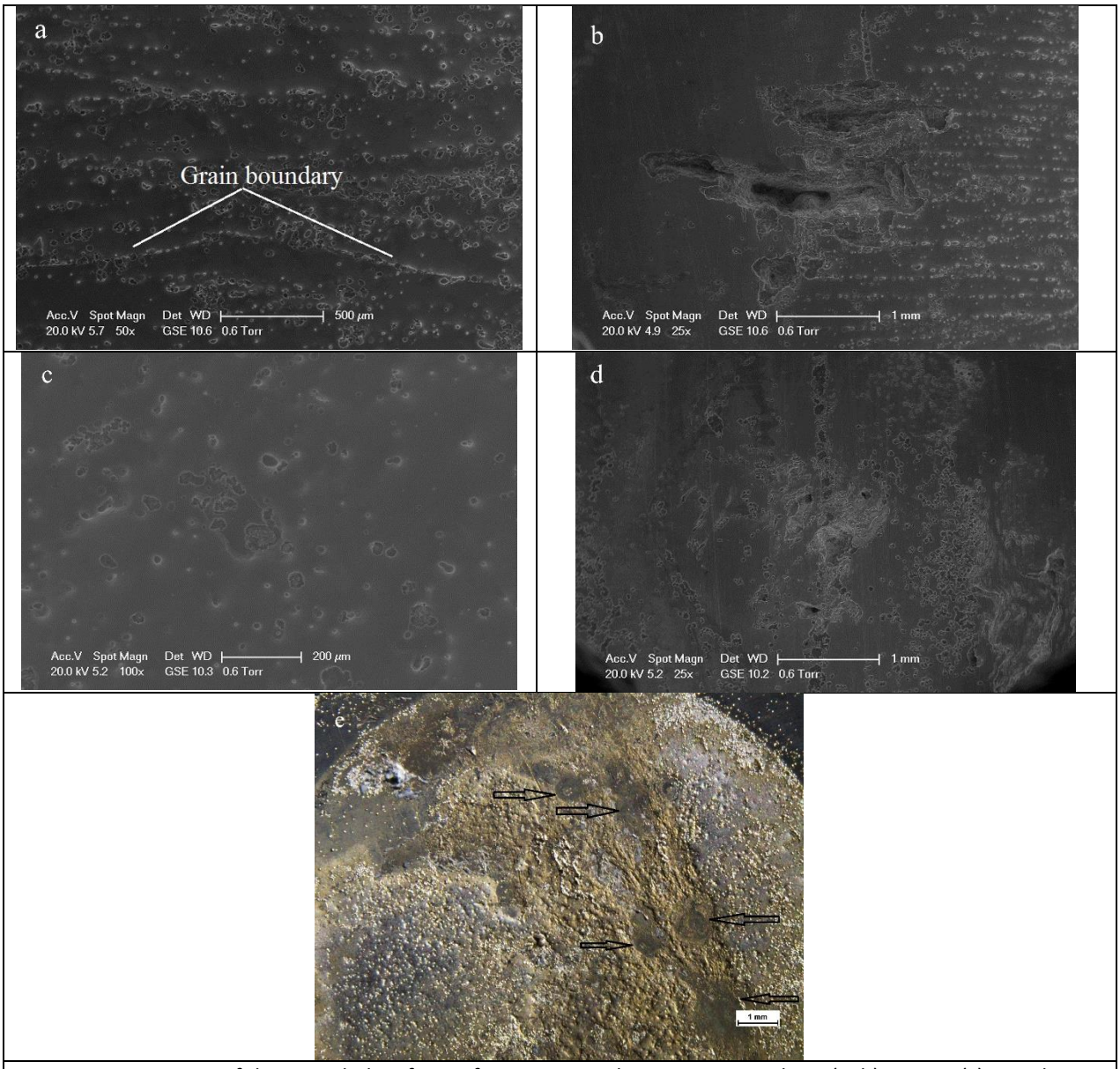

Fig. 10. SEM images of the corroded surfaces after removing the corrosion products (a, b) as cast, (c) FSPed Mg, (d) Mg-HA, (e) OM image of Mg-HA corroded surface after removing the corrosion products.

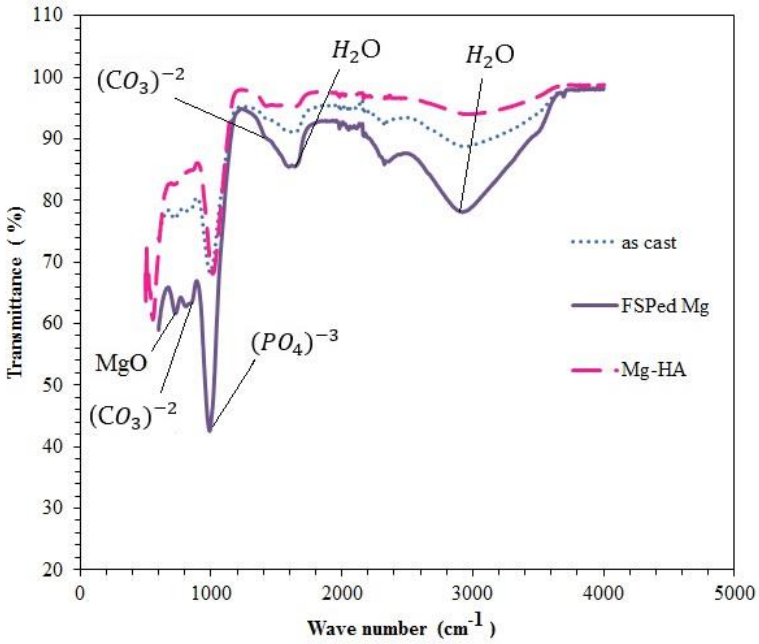

Fig. 11. FTIR analysis of the corrosion products on the surface of the samples immersed in DPBS solution.

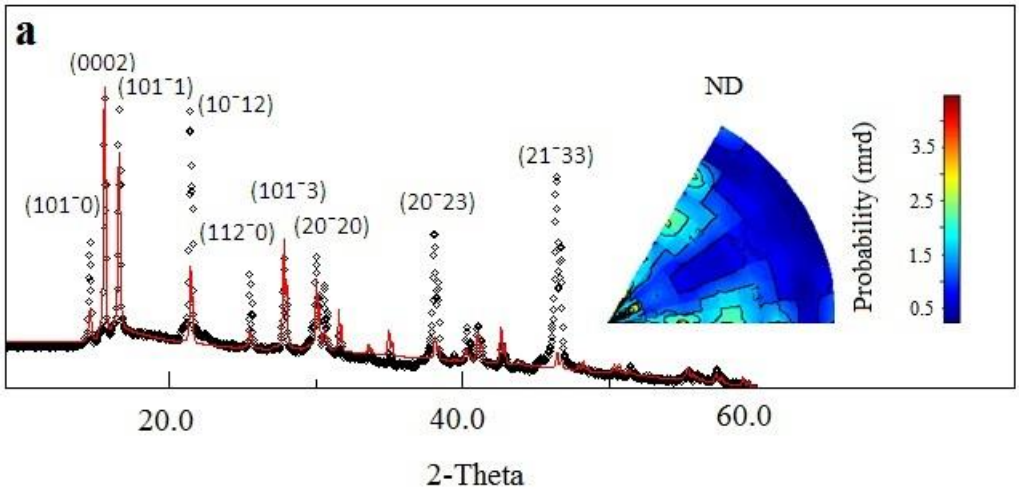

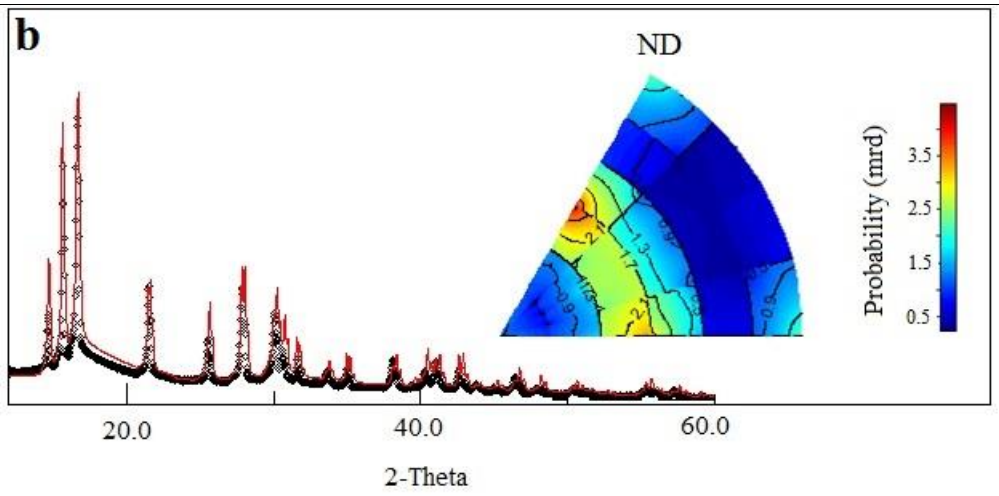

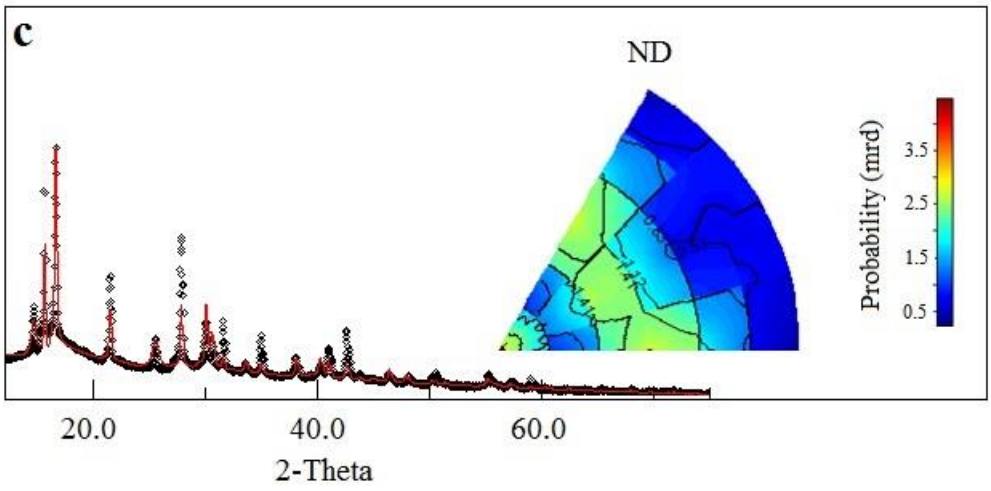

Fig. 12. Pole figures and XRD plots of (a) as cast Mg, (b) FSPed Mg, (c) Mg-HA.

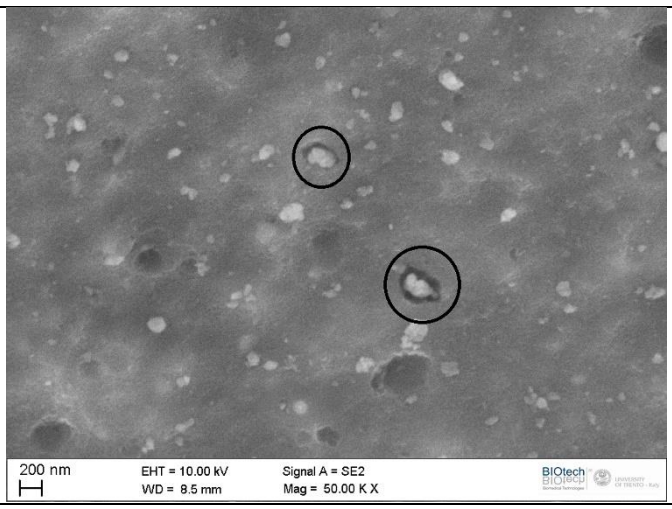

Fig. 13. Corroded surface of Mg-HA composite.